



Dipartimento
di Fisica
e Astronomia
Galileo Galilei



UNIVERSITÀ
DEGLI STUDI
DI PADOVA

Energy calibration of the AN2000 accelerator of LNL and measurement of $^{14}\text{N}(\text{p},\gamma)^{15}\text{O}$ resonance strength at $E_p = 1058 \text{ keV}$

Mariagrazia Lijoi - 2097102 - mariagrazia.lijoi@studenti.unipd.it

Federico Simioni - 2097001 - federico.simioni@studenti.unipd.it

(Dated: May 10, 2024)

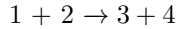
At the National Laboratories of Legnaro there are several accelerators capable of providing different beams in various energy ranges. In particular, the AN2000 could provide proton and alpha beams in a range from 500 keV up to 2 MeV. Its beam energy is determined by the feedback from the bending magnet at the exit of the accelerator. By using different resonance scans, with well-known energy, it is possible to associate the real beam energy with the nominal one according to the magnet field. The resonance scans will also provide other important information about the beam spread and other accelerator parameters. After the characterization of the beam at disposal and the calibration of the accelerator in terms of energy, one can proceed with measurements concerning the reactions of interest. Specifically, in this case, the scan of this reaction has been performed: $^{14}\text{N}(\text{p},\gamma)^{15}\text{O}$, at beam energies around 1058 keV (necessary to obtain the excited state of Oxygen located at 8284 keV), in order to measure the resonance strength and comparing it with previous measurements of the same quantity.

CONTENTS

I. Introduction	1
II. Apparatus & Methods	3
1. Yield	3
2. AN2000 Accelerator	4
A. Magnetic field probes	5
3. LaBr ₃ Detector	5
4. HPGe Detector	6
5. Radioactive sources	7
III. Part 1	8
1. Experimental setup	8
2. Data acquisition	10
3. Data analysis	10
A. Detector energy calibration	10
B. Detector background evaluation	11
C. Accelerator calibration	12
D. Calibration fit	14
E. Comparison	16
IV. Part 2	19
1. Experimental setup	19
2. Data acquisition	21
3. Data analysis	21
A. Detector energy calibration	21
B. Detector background evaluation	22
C. Accelerator calibration	23
D. Strength measurement	25
V. Conclusions	27
References	27
A. Tables	28

I. INTRODUCTION

A generic nuclear reaction typically involves the following situation:



where:

- (1) is the incident particle (referred to as the projectile);
- (2) is the particle being struck (target);
- (3) is the residual product of the projectile after the reaction (p-like);
- (4) is the residual product of the target after the reaction (t-like).

This notation inherently evokes the laboratory-reconstructed situation, where a particle beam represents the projectile directed towards a target (typically solid or gaseous), symbolizing the second particle involved in the aforementioned reaction. This reproducibility in the laboratory is crucial, as determining the reaction cross section (σ) from first principles is not always feasible, thus experiments are necessary in this regard¹. In particular, in the case of stellar reactions (where particles exhibit a velocity distribution following the Maxwell-Boltzmann function) it is more advantageous to consider a measurable quantity closely linked to σ , namely the reaction rate²:

$$r = (\text{Inc. Flux}) \cdot (\text{Eff. Area}) = (N_1 v) \cdot (N_2 \sigma(v)) = N_1 N_2 v \sigma(v)$$

It is important to underline the significance of the quantity $\langle \sigma v \rangle$, which is averaged over all the velocities and is defined as follows [1]:

$$\begin{aligned} \langle \sigma v \rangle &= \int_{v_{\min}}^{\infty} \phi(v) v \sigma(v) dv \\ &= \left(\frac{8}{\pi \mu} \right)^{1/2} \cdot \frac{1}{(kT)^{3/2}} \int_0^{\infty} \sigma(E) E e^{-\frac{E}{kT}} dE \end{aligned}$$

Where $\phi(v)$ represents the Maxwell-Boltzmann distribution, mentioned before relating to particles' velocity distribution inside a star. From this definition, it becomes necessary to distinguish between different types of reactions, each associated with specific approximations, in order to focus only to the one of interest. The initial division concerns the distinction between: Resonant and Non-Resonant reactions. Resonant reactions derive from the presence of discrete nuclear excited states at specific energy levels (described by quantum mechanics); indeed, in such cases, the cross section exhibits distinctive peaks corresponding to energies of the system aligned with them. Focusing on this type of reactions (which are of interest in this work), within this category, it is possible to discern three further types of reactions (the focus will be solely on the first one³):

1. Isolated and Narrow resonances;
2. Broad resonances;
3. Sub-Threshold resonances.

The cross section for the reactions of interest (resonant radiative capture, described by the expression $A(x, \gamma)B$, wherein a photon is emitted) can be decomposed as follows:

$$\sigma_\gamma \propto |\langle E_f | H_\gamma | E_r \rangle|^2 |\langle E_r | H_B | A + x \rangle|^2$$

Where the first part is linked to the compound decay probability while the other to the compound formation probability. Reducing to the case of single isolated resonance, the form the cross section will take is given by the Breit-Wigner expression [1]:

¹ Remembering also that this cross section will depend on the energy of the composite system comprising the incident particles.

² It is indeed necessary to then compare the laboratory measurements with what can be inferred from astronomical observations, remembering that it is interesting to calculate the total nuclear energy released in a stellar plasma, and therefore focusing on the reaction rate is more useful.

³ This is not solely due to the possibility of obtaining good results with the instrumental apparatus, but it also holds practical implications. As will be seen later, the first concern of this work will be to calibrate the accelerator in terms of energy, and to achieve this it is necessary to utilize isolated and narrow resonances. This is because of the low uncertainty that can be associated with them, resulting in a more reliable calibration.

$$\sigma(E) = (\pi\lambda) \cdot \left(\frac{2J+1}{(2J_1+1)(2J_2+1)} \right) \cdot \left(\frac{\Gamma_a \Gamma_b}{(E-E_r)^2 + (\Gamma/2)^2} \right)$$

Where the first term in brackets represents the geometrical factor, the second is the spin factor (the so-called ω^4), and the third is a strongly energy-dependent term encompassing the probabilities of compound formation and decay via entrance and exit channels, with E_r and Γ representing the resonance's energy and total width respectively. Utilizing this definition in the aforementioned expression of $\langle\sigma v\rangle$, and assuming additionally that the resonance is narrow ($\Gamma \ll E_r$ as depicted in FIG. 1, Maxwell-Boltzmann distribution and partial widths assumed constant), the following expression is obtained:

$$\langle\sigma v\rangle_{12} = \left(\frac{2\pi}{\mu_{12}kT} \right)^{3/2} \cdot \hbar^2 \cdot (\omega\gamma)_R \cdot e^{-\frac{E_r}{kT}}$$

In this final equation⁵, there is a particular unknown value that stands out, namely $(\omega\gamma)_R$ also defined as the reaction's resonance strength⁶ and its determination is the objective of this study. The evaluation of this parameter allows to characterize the reaction of interest, that in the present study is: $^{14}\text{N}(p,\gamma)^{15}\text{O}$ (with a beam energy of 1058 keV). The latter is of particular relevance in the CNO cycle as it is the slowest, and so it determines the rate of the entire cycle. To achieve this it will be necessary to work on the entire apparatus to calibrate it in preparation for the measurement.

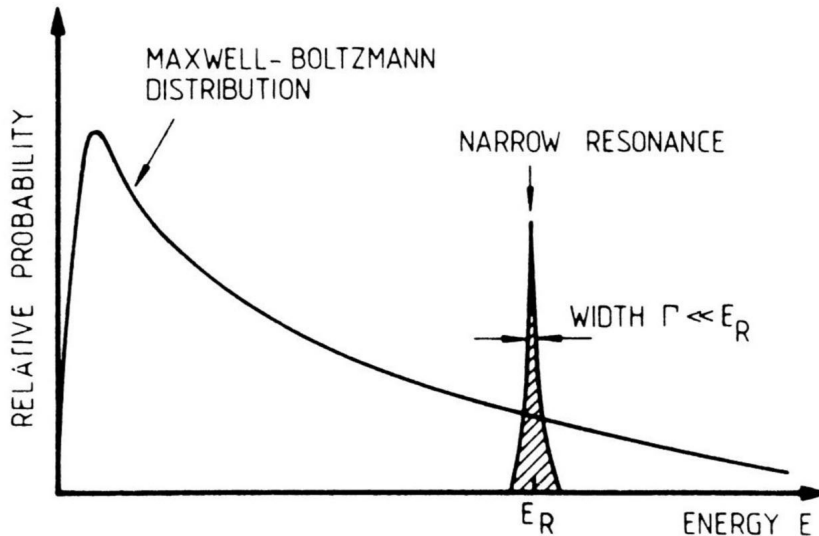


FIG. 1 Behavior as a function of Energy of the Maxwell-Boltzmann Distribution and of a Narrow Resonance Positioned at E_R [7].

⁴ J represents the spin of CN's state, J_1 the spin of the projectile and J_2 the spin of the target

⁵ In reference to what was mentioned earlier, here it is possible to observe how small uncertainties in E_r lead to significant uncertainties in reaction rate.

⁶ In this term γ stands for $\frac{\Gamma_a \Gamma_b}{\Gamma}$

II. APPARATUS & METHODS

1. Yield

For both phases of the experiment, what has actually been determined from the acquisitions is the yield, Υ , as this parameter is closely related to the reaction rate and consequently to the cross section of the considered reaction. The yield can be simply defined as:

$$\Upsilon = \frac{\text{total number of nuclear reactions}}{\text{total number of incident beam particles}} = \frac{N_R}{N_b} \quad (1)$$

In particular, the function of the yield versus the varying beam energy (incident particles) defines the excitation function. Furthermore, it is possible to define Υ in a way that more explicitly highlights its connection with σ . It is hypothesized that the target is hit by a beam with initial energy E_0 , and the target is imagined to be divisible into many slices of infinitesimal thickness equivalent to a beam energy loss of ΔE_i (where i stands for the i -th slice). This translates into the following expression:

$$\Delta\Upsilon_i = \frac{N_{R,i}}{N_b} = \sigma_i \cdot \frac{N_{t,i}}{A} = \sigma_i N_i \Delta x_i \quad (2)$$

Where $N_{t,i}$ is the number of scattering centers in the i -th slice of the target, A is the area of intersection between the beam and the target, and N_i is the density of scattering centers in the i -th slice of the target. Integrating over the entire thickness of the target:

$$\Upsilon(E_0) = \int \sigma(x) N(x) dx = \int_{E_0 - \Delta E}^{E_0} \frac{\sigma(E)}{\epsilon(E)} dE, \text{ where } \epsilon(E) = -\frac{1}{N} \frac{dE}{dx} \quad (3)$$

where ΔE is the thickness of the target in terms of energy units, and $\epsilon(E)$ is the stopping power in the case of a pure target. When the target is considered as a compound of n_X active nuclei and n_Y inactive nuclei, it is necessary to use the effective stopping power:

$$\epsilon_{eff} = \epsilon_X + \frac{n_Y}{n_X} \epsilon_Y \quad (4)$$

It has already been emphasized that in both phases of the experiment, narrow resonances of specific reactions will be exploited. For this reason, σ can be approximated by a Breit-Wigner distribution and consequently yielding [4]:

$$\Upsilon(E_0) = \frac{\lambda_r^2 \omega \gamma}{2\pi \epsilon_r} \left[\arctan \left(\frac{E_0 - E_r}{\Gamma/2} \right) - \arctan \left(\frac{E_0 - E_r - \Delta E}{\Gamma/2} \right) \right] \quad (5)$$

where λ_r is the de Broglie wavelenght, ϵ_r is the stopping power at the resonance energy E_r . Doing some algebra, it is possible to obtain this two interesting values:

$$E_{0,max} = E_r + \frac{\Delta E}{2} \quad (6)$$

$$\Upsilon_{max} = \Upsilon(E_{0,max}) = \frac{\lambda_r^2 \omega \gamma}{\pi \epsilon_r} \arctan \left(\frac{\Delta E}{\Gamma} \right) \quad (7)$$

with $E_{0,max}$ the position of the maximum and Υ_{max} the maximum yield.

Looking at this example (see FIG. 2), one can observe how the shape of the yield curve changes in relation to the width of the target compared to the Γ of considered resonance.

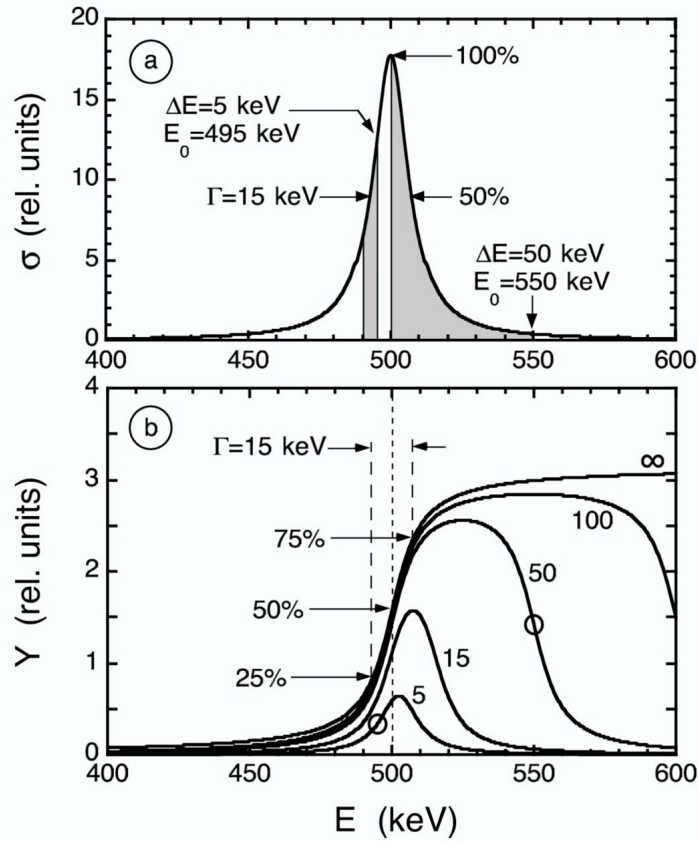


FIG. 2 Yield curve for a Breit–Wigner resonance with energy-independent partial widths [4].

Focusing on the circumstances of the experiment conducted, in both phases the target is approximated as infinitely thick, i.e. $\Delta E \rightarrow \infty$, thus the following approximations are obtained:

$$\Upsilon_{\Delta E \rightarrow \infty}(E_0) = \frac{\lambda_r^2 \omega \gamma}{2\pi \epsilon_r} \left[\arctan \left(\frac{E_0 - E_r}{\Gamma/2} \right) + \frac{\pi}{2} \right] \quad (8)$$

$$\Upsilon_{max, \Delta E \rightarrow \infty} = \frac{\lambda_r^2 \omega \gamma}{2 \epsilon_r} \quad (9)$$

All of this is highly favorable for both objectives of this study. In fact, in order to obtain the necessary values for the calibration curve of the AN2000 accelerator, it is trivially understood that the energy value at which the curve bends coincides with E_r . Lastly, referring to the last equation presented, it is noticeable that by simply rearranging it, one can easily obtain the quantity $\omega \gamma$, namely the resonance strength of interest [4].

2. AN2000 Accelerator

The AN2000 is an accelerator of electrostatic-type with a voltage terminal of 2 MV. The whole accelerator facility (i.e. accelerator with internal ion source, beam channels and all measurements points) is installed in a single experimental room⁷. The smaller output energy available by such a compact-size accelerator makes it an ideal facility to promote nuclear reaction events with the first layers of target materials. AN2000 is therefore primarily dedicated to the detailed investigation of materials surface properties, as well as to induce, on request, physical-chemical properties

⁷ <https://www.lnl.infn.it/en/an2000-2/>

modifications on surface materials for a variety of purposes and applications. By means of this accelerator, detailed measurements for the elemental composition analysis of any material can be performed, by bombarding samples and identifying, through appropriate detection techniques, the particles or radiation which are produced in the beam interaction with material. Protons or helium beams are used to probe the samples. Material analysis with this accelerator unveils the chemical composition and distribution profiles of the various constituent elements at various depths. Such nuclear, non-destructive, techniques are ideal for other fields of investigation such as archeology, for dating finds (solid samples), and environmental physics, for determining with great precision the contamination level and pollution in air and water.

The physics principle behind the ions beam generation and transport is identical to that of any single-stage Van de Graaff electrostatic-type accelerators. The entire facility can be schematically represented as in FIG. 3.

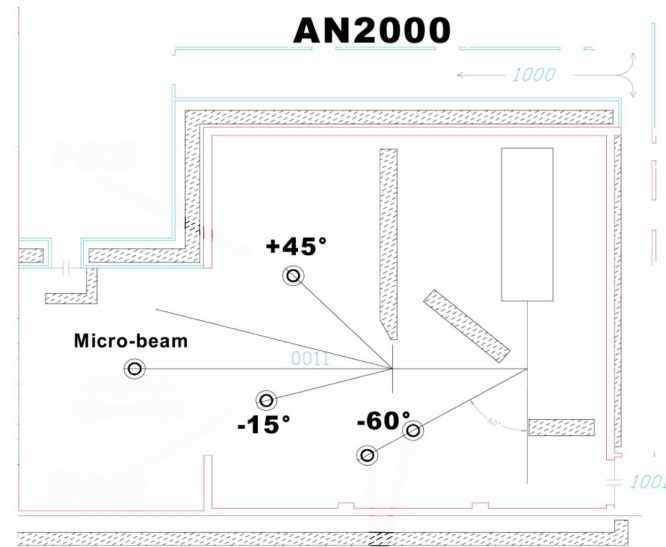


FIG. 3 Schematic representation of entire AN2000 facility [8].

During the experiment, it was primarily used the line positioned at -60° , and then for measuring the resonance strength, it was employed the one marked at -15° [8].

A. Magnetic field probes

In this brief description of the accelerator, it is important to mention the tools utilized for measuring the magnetic field responsible for bending the particle beam⁸. For this purpose, reference was made to an NMR probe, which provides values with 9 significant digits (10 kGauss as the most significant one), and on a Gaussmeter, providing values with 4 significant digits (1 kGauss as the most significant one). In particular, the latter was employed only to confirm the values reported by the former. Regarding the error of the NMR measurements, it was considered equals to $\frac{ptl}{\sqrt{12}}$, where ptl consists of the third least significant digit (thus $\sigma_{NMR} = 0.000003 \cdot 10^4$ Gauss). This choice is motivated by the fact that during the measurements, the values obtained from the probe were not constant but constantly oscillated up to the third digit.

3. LaBr₃ Detector

During this experiment, LaBr₃ scintillators were utilized. These belong to the category of inorganic scintillators and exhibit several characteristics that make them particularly favored compared to various alternatives.

- Firstly, they possess a high effective atomic number (Z_{eff}) and density, which makes them convenient for gamma detection;

⁸ See the first part of Chapter III related to the initial experiment for further details.

- They have a low decay time, making them preferable in situations requiring high counting rates or fast timing.
- The emitted radiation wavelengths are well matched with common photocathodes.
- They offer excellent energy resolution (around 3% at 662 keV), superior to alternatives in the same category.
- Commercially available.
- Constant light yield and energy resolution over a wide range of temperatures.
- Good resistance to damage caused by radiation exposure to high doses of gamma rays and protons.

Despite these numerous advantages, there are also some drawbacks. The first concerns intrinsic radioactivity (estimated around 1-2 decays/cm³.s), due to the presence of ¹³⁸La and ²²⁷Ac within the material. This can be inconvenient for spectra with low counts, where it is necessary to detect radiation just above the background. The ¹³⁸La primarily decays in two ways: through electron capture to ¹³⁸Ba (66.4%) with gamma ray emission at 1436 keV coinciding with a 32 keV X-ray due to Ba rearrangements, or through beta decay (33.6%) with a Q-point at 255 keV and coinciding with a gamma ray at 789 keV. Observing a typical background spectrum obtained with these types of detectors, one can observe:

- A trapezoidal-shaped continuum between 750 keV and 1000 keV, due to the sum from ¹³⁸La beta decay;
- A peak at 1468 keV due to the sum from emissions following electron capture;
- A structure between 1750-3500 keV, resulting from alpha decays associated with the ²²⁷Ac decay chain.

Another typical drawback of this type of detector concerns the hexagonal crystal structure, which can lead to anisotropic thermal expansion with consequent internal stresses as crystals cool after growth. This, combined with the fact that LaBr₃(Ce) is more hygroscopic than NaI(Tl), justifies the particular attention that must be paid during manufacturing processes (which also justifies the very high price). Finally, lanthanum halides are not particularly suitable for pulse shape discrimination. An example of the spectrum of Lanthanum Bromide is represented in FIG. 10, wherein all the aforementioned components can be observed [5].

4. HPGe Detector

During the calibration phase of the AN2000 accelerator, an High Purity Germanium (HPGe) detector was also used during acquisitions. The latter is essentially a semiconductor detector, and its operation is based on the band structure of semiconductors, exploiting properties related to the semiconductor case (see FIG.4). In particular, in this field, the effects of p- or n-doping of the semiconductor are often used to amplify the characteristics necessary for specific measurements.

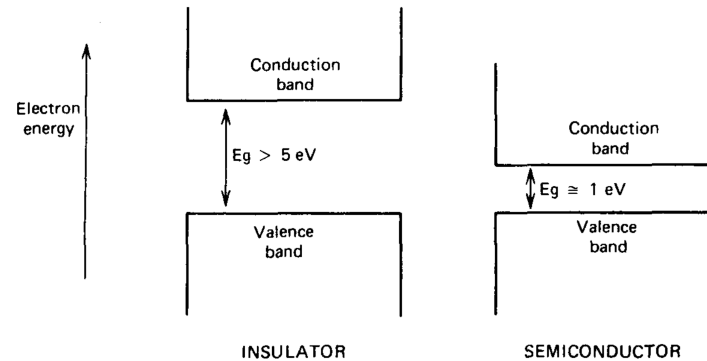


FIG. 4 Band structure of insulators and semiconductors [5].

The use of HPGe for gamma spectroscopy has several advantages:

- Excellent energy resolution;
- Very low noise;
- It is a very dense material;
- Its radiation length is very small;
- It has few impurities, consequently its active volume is larger.

However, HPGe also has its limitations. Indeed, having a very small energy gap (0.7 eV), it cannot operate at room temperature because a significant leakage current would be induced, compromising its excellent energy resolution. For this reason, HPGe is contained within a liquid nitrogen cooling system. Furthermore, having high energy resolution, it has a discrete efficiency that depends greatly on the geometric configuration of the experiment. Finally, this detector has a low time resolution because it depends on the charge collection time [5] [3].

5. Radioactive sources

In order to do the energy calibration of the detectors used during both phases of the experiment, the following radioactive sources were employed:

1° phase: AN2000 Calibration		2° phase: Resonance strength	
Element	Recognition code	Element	Recognition code
⁶⁰ Co	493/5c	²² Na	493/8c
¹³⁷ Cs	473c	¹³⁷ Cs + ¹³⁷ Ba	397/5c

TAB. 1 Radioactive sources from INFN LNL used for detector energy calibration.

III. PART 1

The first part of the experiment was dedicated to the calibration of the AN2000 accelerator. This operation is necessary because the particle beam is accelerated by a static potential, and energy selection occurs through the use of a dipolar magnet, which bends the beam and selects in energy according to the following relationship [4].

$$B = \sqrt{2mc^2E + E^2} \cdot \frac{k}{q}$$

In principle, therefore, starting from the value indicated by the NMR probe, one should already be able to determine the energy of the incident beam, and indeed, in the laboratory, there was already a conversion table for Magnetic Field (NMR probe value) - Energy (kV)⁹. However, over time, some parameters of the facility may change slightly, and with them, the actual calibration of the entire apparatus, hence the reason for these measurements to confirm or correct the official calibration (and observe any changes between different measurement days). For this purpose, a technique for calibrating the accelerator involves generating well-known resonance reactions, preferably isolated and narrow, to facilitate their observation¹⁰. Since these reactions occur at specific energies, establishing the correspondence between the measured parameters (see NMR probe) within the accelerator's setting and the resonance energy will be facilitated. In the present experiment, three resonances¹¹ have been exploited, generated by the two reactions listed below:

- $^{27}\text{Al}(\text{p},\gamma)^{28}\text{Si}$: Concerning the first reaction, it is also involved within the NeNa and MgAl cycles (alternative to H burning¹²). This is a resonant reaction that can be induced with a proton beam of $E_p = 991.86 \pm 0.03$ keV in the laboratory reference frame (incident on an aluminum target, as inferred from the reaction). In this reaction, a gamma ray of $E_\gamma = 1779$ keV is produced, and the resonance width is $\Gamma_{\text{CM}} = 0.070 \pm 0.014$ keV;
- $^{27}\text{Al}(\text{p},\text{p}'\gamma)^{27}\text{Al}$: Regarding the second reaction, it can generate two resonances, one at a proton beam of $E_{p1} = 1664.4 \pm 0.2$ keV and the other at $E_{p2} = 1683.57 \pm 0.13$ keV, both of which yield a gamma ray of $E_\gamma = 843$ keV. However, the resonance width in the first case is $\Gamma_{\text{CM1}} = 0.45 \pm 0.05$ keV whereas in the second $\Gamma_{\text{CM2}} < 0.2$ keV.

1. Experimental setup

The experimental apparatus comprised the following components:

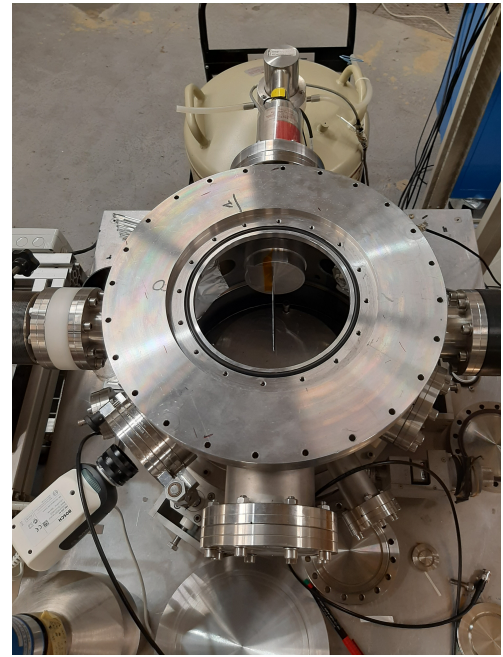
- The AN2000 accelerator (the entire facility, including magnets for bending the beam to select energy, and probes for measuring the magnetic field);
- An intermediate scattering chamber positioned at -60 degrees;
- An Aluminum target consisting of a 0.1 mm thick sheet with 99% purity;
- An HPGe detector and a Lanthanum Bromide detector.

⁹ The unit of measure would represent a potential, which in itself is not energy. However, when multiplied by the charge state of the particles accelerated in the beam, it yields the energy of the incident particles.

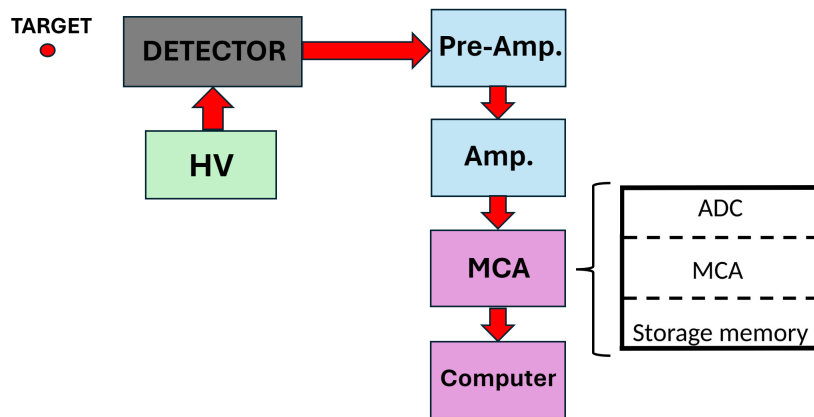
¹⁰ At higher energies than 2 MeV, (p,n) reactions with a threshold are used.

¹¹ All involving proton beam. To some extent this can be considered a calibration in energy of the accelerator considering only protons.

¹² Valid for second-generation stars, where stellar temperatures are higher than those for the quiescent CNO cycle. Both of these mentioned cycles do not play a significant role as energy sources within a star (due to the high Coulomb barrier), but they do play a significant role in the nucleosynthesis of elements ranging from ^{20}Ne to ^{27}Al .

**FIG. 5** Detector setup.**FIG. 6** Scattering chamber with the Aluminum target inside.

As previously described, the AN2000 is an electrostatic accelerator capable of accelerating both protons and Helium nuclei. For this experiment, it enabled us to generate a proton beam with energies below 2 MeV (consider the energies mentioned earlier when listing the reactions of interest). To measure the resonances discussed previously, the yield of the reaction was assessed, initially defined as the number of reactions per number of incident particles. To measure the number of these incident particles, a Digital current integrator from ORTEC (model 439) was used, connected to an integrated counter in another ORTEC module (928 EASY-NIM Multi-Function MCA/Counter/Timer/Rate Meter). These devices together maintained a count of the integrated charge starting from the current represented by the beam (each count corresponding to a charge of 10^{-10} C). These protons were then accelerated towards the target located inside the previously listed scattering chamber, and the reactions (represented by the characteristic gamma rays emitted from the populated resonant states, forming the numerator of the yield) were detected by the provided detectors, arranged as shown in FIG. 5. The Lanthanum Bromide was placed directly above the scattering chamber, while the HPGe, requiring cooling by liquid nitrogen, was positioned horizontally within one of the entrance channels of the employed scattering chamber (closest to the target). Both detectors were equipped with an HV power supply (to the HPGe to form the depletion region, to the Lanthanum Bromide to power the photomultiplier), and the electronic chain is described in the schematic representation of FIG. 7.

**FIG. 7** Schematic representation of the analog chain.

As can be observed, both detectors were connected to two modules that functioned as pre-amplifiers and amplifiers. Specifically, a Spectroscopic Amplifier from CAEN (Model N968) and an Amplifier from ORTEC (Model 572) were utilized. These were then directly connected to the control room, which housed two modules: the previously mentioned ORTEC Model 928, to which the HPGe detector was connected, while the lanthanum detector was connected to an ORTEC Model ASPEC-927 Dual Input MCB, and both serving as ADC and MCA, directly connected to a computer. Regarding the Data Acquisition (DAQ) system, the interaction between these modules and the computer was managed using MAESTRO (in PHA Acquisition Mode), a software package provided by ORTEC. MAESTRO functions as a multichannel analyzer (MCA) emulation software and is also utilized for data acquisition. Finally, after arranging everything, including the target, the entire chamber was set into vacuum. For this purpose, a combination of primary (scroll pump) and secondary (turbomolecular pump) stage pumps was employed, achieving a vacuum within the chamber set to $10^{-6} - 10^{-7}$ mBar.

2. Data acquisition

The experiment consisted of a resonance scan in which the energy of the beam was varied in small increments, and the gamma spectrum was acquired at each step to obtain the yield. The following procedure was adopted:

- Initially, the parameters of the accelerator were set such that the beam energy was close to that of the resonance of interest, in accordance with conversion tables provided by the laboratory.
- Subsequently, the scan started, and data were collected for each run, with the beam energy incrementally increased by a few keV.
- By utilizing the previously mentioned software, a preliminary analysis was conducted to identify the rise of the yield (obtained by integrating the peak corresponding to the gamma of interest), which guided decisions on whether to increase or decrease the energy steps.

The data acquisition process lasted two days, during which the following activities were carried out:

- On the first day, after setting up the apparatus and setting the accelerator to an energy below that of the first mentioned resonance, an initial scan was conducted. Following the successful completion of this initial measurement, scans for the other two resonances (1664 and 1684 keV) were performed in the afternoon.
- On the second day, issues with the cooling system of the magnet were encountered, restricting data collection to the morning and thus limiting the scans to the reactions at 1664 and 1684 keV only. Following this, the entire accelerator had to be shut down, and a simple measurement with sources for energy calibration of the detectors was carried out.
- Overnight, background measurements for the Lanthanum detector were conducted.

3. Data analysis

A. Detector energy calibration

The first step of data analysis is the energy calibration of both detectors (HPGe and LaBr_3), in order to translate the units of the data acquisition system (ch) into the ordinary energy units (keV). For the latter purpose, the acquired spectra of two radioactive sources, ^{60}Co and ^{137}Cs , were used. Then a Gaussian fit was performed for every peak, in order to get the centroids and their errors¹³; these values are shown in TAB. 2:

	HPGe [ch]	LaBr_3 [ch]
^{137}Cs 662 keV	1006.06 ± 0.02	227 ± 1
^{60}Co 1173 keV	1783.80 ± 0.03	401 ± 1
^{60}Co 1332 keV	2025.87 ± 0.03	454 ± 1

TAB. 2 Centroids of every peak for each source.

¹³ In this case the evaluation of the background for both detectors is not so important, because the only useful value of the fit is the centroid.

Then a linear fit was executed for both detectors, such that:

$$E_\gamma = a + bN_{ch}, \quad (10)$$

where E_γ represents the known values¹⁴ of photopeak energies for the two sources, N_{ch} is the position of the peak centroid in the units of the DAQ system and a and b are the fit parameters.

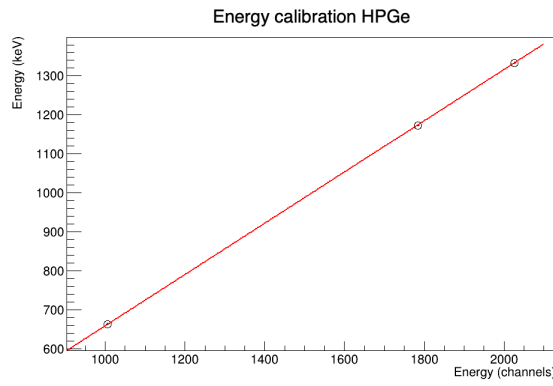


FIG. 8 Energy calibration fit of HPGe detector.

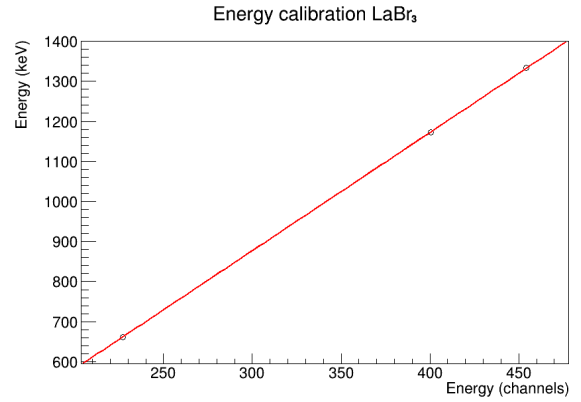


FIG. 9 Energy calibration fit of LaBr₃ detector.

The obtained fit parameters are shown in TAB 3.

	Slope [keV/ch]	Intercept [keV]
HPGe	0.65779 ± 0.00002	-0.13 ± 0.03
LaBr ₃	2.95 ± 0.01	-8 ± 5

TAB. 3 Parameters of energy calibration of both detectors.

B. Detector background evaluation

In order to obtain a reliable value of the yield Υ , it is necessary to determine a reliable value of the integral of the area under the peak of the studied resonances (~ 1778 keV or ~ 843 keV). These fall within a critical energy range concerning the intrinsic background of the LaBr₃ detector. For this reason, as a first step, the background histogram was manually subtracted from all spectra acquired by the LaBr₃ during each data acquisition. An example¹⁵ of the process is shown in FIG. 10.

Instead, as described earlier, the HPGe detector has very high energy resolution and almost negligible background. Consequently, for each acquired spectrum, it was assumed that the background followed a linear trend, and its contribution was subtracted during various fitting operations on the peak of the studied resonances (see FIG. 11).

¹⁴ The known values of the emission energies of ⁶⁰Co and ¹³⁷Cs are available on web site:http://www.lnhb.fr/nuclides/Co-60_tables.pdf, http://www.lnhb.fr/nuclides/Cs-137_tables.pdf

¹⁵ In this instance, the spectrum shown in blue was obtained from the first resonance, as indicated by the presence of the peak at 1778 keV. Conversely, the spectrum displayed in red was obtained during the night between the two days of measurements.

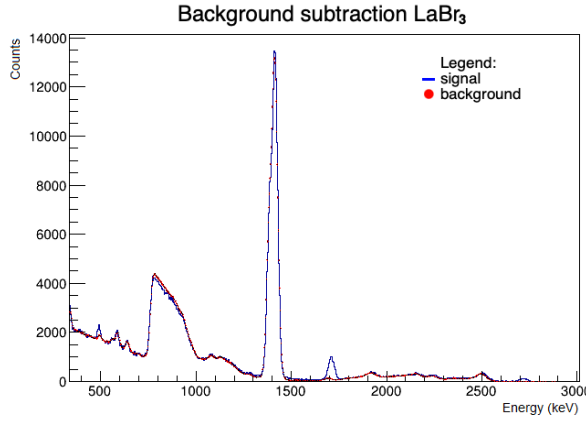


FIG. 10 LaBr₃ background subtraction from one of the acquired spectrum.

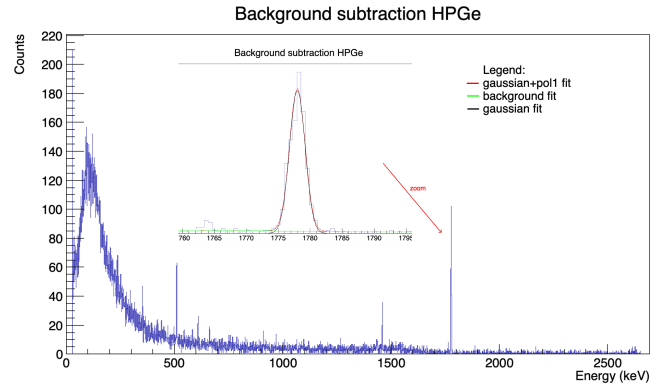


FIG. 11 HPGe background subtraction from one of the acquired spectrum.

C. Accelerator calibration

As previously described, the energy calibration of the AN2000 accelerator was conducted by exploiting the well-known resonances of two reactions defined in the introduction of the section III. In both cases, what was actually calculated during the data analysis was the Υ (see II.1) which experimentally can be defined as follows:

$$\Upsilon = \frac{N_{peak}}{N_c} \quad (11)$$

where N_{peak} is the integral of the peak of the emitted photon during the considered resonance, while N_c is the reprocessed value given by the ORTEC counter for each acquisition. In fact, the latter returns the value of the charge on the target in 10^{-10} C, therefore it needs to be normalized and made dimensionless, in formula:

$$N_c = \frac{\text{counter} \cdot 10^{-10}}{1.6 \cdot 10^{-19}} \quad (12)$$

In particular the error of the ORTEC counter can be considered negligible, so the only error source for the Υ derives from the calculation of the integral from each histogram.

Starting from the reaction $^{27}\text{Al}(\text{p},\gamma)^{28}\text{Si}$, the Υ was calculated by analyzing the photon peak of about 1778 keV for each spectrum acquired during the scan of that specific resonance and for both detectors (see appendix A). Then, the Υ values obtained were plotted as a function of the corresponding NMR probe values, and a fit was performed with a single arc-tangent function:

$$f(x) = a + b \cdot \text{atan}(c \cdot (x + d)) \quad (13)$$

because in this case there was a single photon emitted at one specific energy of the proton beam and the target was considered infinitely thick.

	a	b	c [1/nmr]	d [nmr]	χ^2
HPGe	(2.36±0.07)E-13	(5.9±0.5)E-15	(2.8±1.0)E+4	(-1.62842±0.00011)E-1	4.5
LaBr ₃	(1.242±0.004)E-11	(2.99±0.03)E-12	(3.56±0.15)E+4	(-1.628460±0.000001)E-1	79

TAB. 4 Single arc-tangent fit parameters for both detectors.

Observing TAB. 4, it can be noted that in the case of data analysis from the HPGe detector, the χ^2 value is quite in line with Ndof, therefore the errors associated with the fitted points can be considered adequate. However, in the case of the LaBr₃ detector, the χ^2 value is higher compared to the degrees of freedom, indicating an underestimation of the errors related to the measurements derived from this detector. This difference, which will also be reflected in subsequent calculations, is probably due to the different background subtraction process that affects the error associated with the calculated integrals. In fact, in the case of HPGe, there is a propagation of errors associated with

the parameters of the fits performed on the peak, while in the case of LaBr_3 , only the errors determined by the ROOT software were used in the calculation of the integrals.

In addition **d** represents the flex of the arc-tangent, i.e. the value E_p at which resonance occurs, while **c** is a parameter from which the width of the resonance can be derived. The other two parameters represent some intrinsic characteristics of the function, as the offset or the rise steepness.

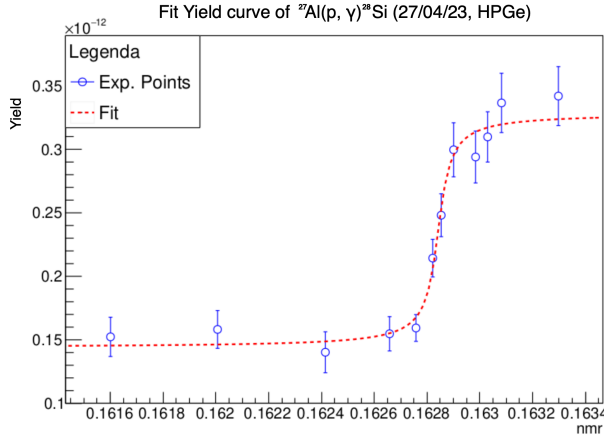


FIG. 12 Single arc-tangent fit of the Yield curve for $E_\gamma=1778$ keV (HPGe, 27/04/23).

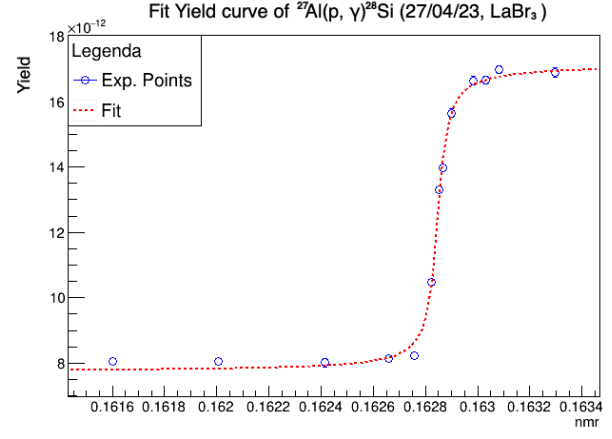


FIG. 13 Single arc-tangent fit of the Yield curve for $E_\gamma=1778$ keV (LaBr_3 , 27/04/23).

Instead, regarding the reaction $^{27}\text{Al}(\text{p}, \text{p}'\gamma)^{27}\text{Al}$, the Υ was calculated by analyzing the photon peak of about 843 keV for each spectrum acquired during the scan of that specific resonance and for both detectors (see appendix A). Afterwards, a fit was performed of the obtained Υ as a function of the NMR probe values, using a double arc-tangent function:

$$f(x) = a + b \cdot \text{atan}(c \cdot (x + d)) + e + f \cdot \text{atan}(g \cdot (x + h)) \quad (14)$$

because in this case there was a photon of the same energy emitted at two different energy of the proton beam and the target was considered always infinitely thick.

Parameters	HPGe (27/04/23)	HPGe (28/04/23)	LaBr ₃ (27/04/23)	LaBr ₃ (28/04/23)
a	(10±2)E-13	(1.1±0.3)E-12	(3.21±0.13)E-11	(3.23±0.02)E-11
b	(3.4±0.2)E-13	(3.2±0.3)E-13	(1.281±0.013)E-11	(1.42±0.02)E-11
c [1/nmr]	(3.5±1.7)E+4	(1.1±0.9)E+5	(4.7±0.5)E+4	(2.9±0.2)E+4
d [nmr]	(-2.10687±0.00008)E-1	(-2.10747±0.00003)E-1	(-2.10683±0.00001)E-1	(-2.10760±0.00002)E-1
e	(3±3)E-12	(2.6±0.3)E-12	(1.021±0.013)E-10	(1.023±0.002)E-10
f	(7.9±0.5)E-13	(7.6±0.5)E-13	(3.01±0.03)E-11	(2.84±0.03)E-11
g [1/nmr]	(2.7±0.7)E+4	(5±2)E+4	(3.10±0.11)E+4	(7.3±1.0)E+4
h [nmr]	(-2.11912±0.00006)E-1	(-2.11988±0.00009)E-1	(-2.119060±0.00009)E-1	(-2.119940±0.000013)E-1
χ^2	6.5	7.2	218	29

TAB. 5 Double arc-tangent fit parameters for both detectors and days.

In particular **d** and **h** represent the two flexes of the double arc-tangent, while **c** and **g** are the parameters related to the widths of the resonances.

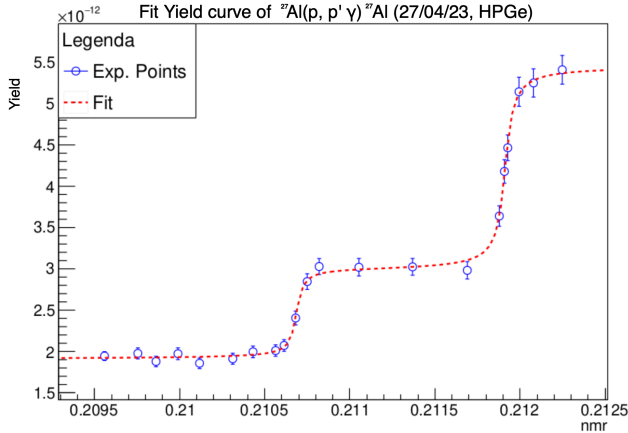


FIG. 14 Double arc-tangent fit of the Yield curve for $E_\gamma=843$ keV (HPGe, 27/04/23).

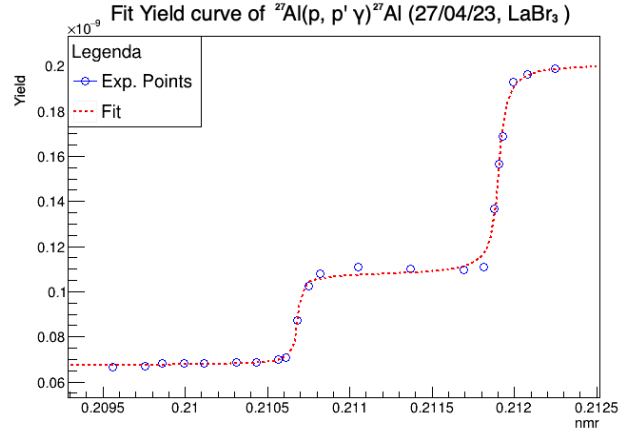


FIG. 15 Double arc-tangent fit of the Yield curve for $E_\gamma=843$ keV (LaBr₃, 27/04/23).

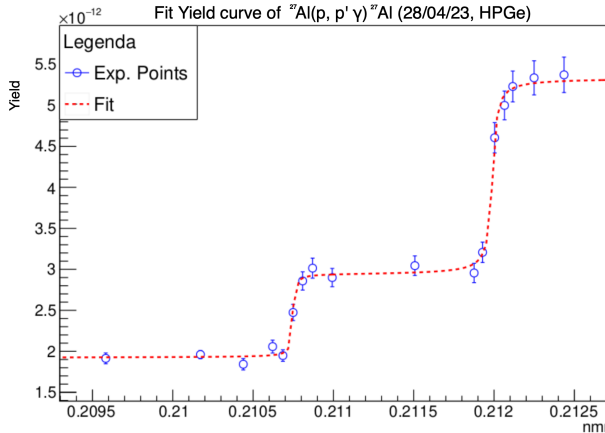


FIG. 16 Double arc-tangent fit of the Yield curve for $E_\gamma=843$ keV (HPGe, 28/04/23).

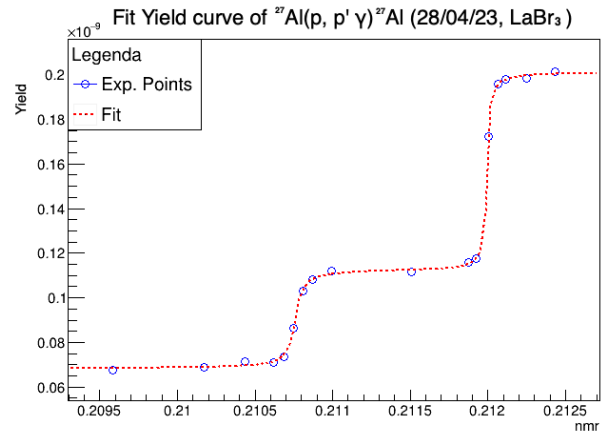


FIG. 17 Double arc-tangent fit of the Yield curve for $E_\gamma=843$ keV (LaBr₃, 28/04/23).

D. Calibration fit

Upon achieving these fits, as said before it was then possible to identify the inflection points related to the yields of each resonance, namely the NMR values of resonance energies. These points facilitated the energy calibration of the accelerator, distinguished by detector and by day¹⁶, as shown in FIG. 18, 19, 20 and 21 with the fit parameter values listed in TAB. 6. Given the expression that relates the curvature magnetic field to the beam energy (refer to the introduction of Part 1), a linear fit was considered a good approximation.

Parameters	HPGe (27/04/23)	HPGe (28/04/23)	LaBr ₃ (27/04/23)	LaBr ₃ (28/04/23)
Slope [keV/nmr]	$(1.4085 \pm 0.0004)E+4$	$(1.54 \pm 0.02)E+4$	$(1.4082 \pm 0.0004)E+4$	$(1.553 \pm 0.019)E+4$
Intercept [keV]	$(-1.3017 \pm 0.0008)E+3$	$(-1.59 \pm 0.05)E+3$	$(-1.3014 \pm 0.0008)E+3$	$(-1.61 \pm 0.04)E+3$
χ^2	47.9	-	51.9	-

TAB. 6 Parameters of the linear fit representing the Accelerator energy calibration.

¹⁶ They were kept separate as we do not know a priori whether they are compatible with each other.

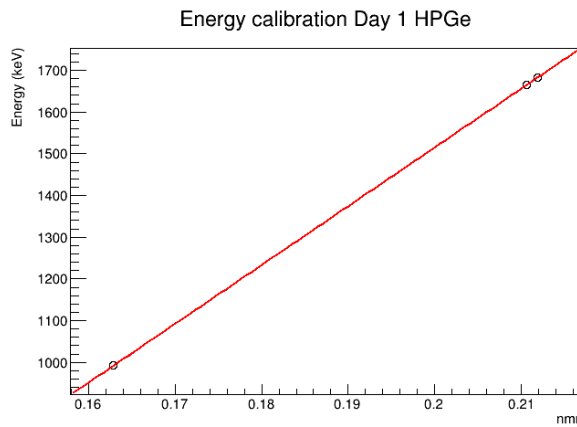


FIG. 18 Accelerator energy calibration (using HPGe, on 27/04/23).

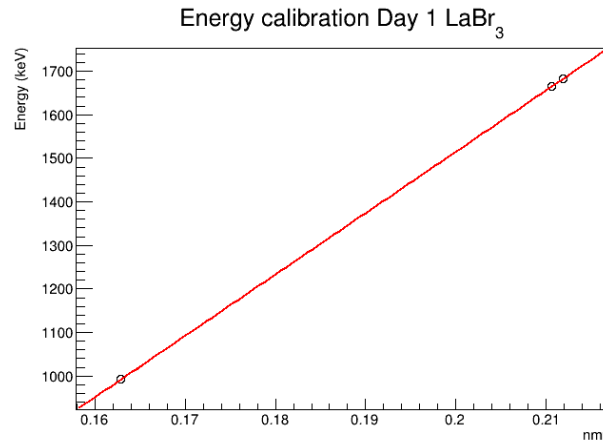


FIG. 19 Accelerator energy calibration (using LaBr₃, on 27/04/23).

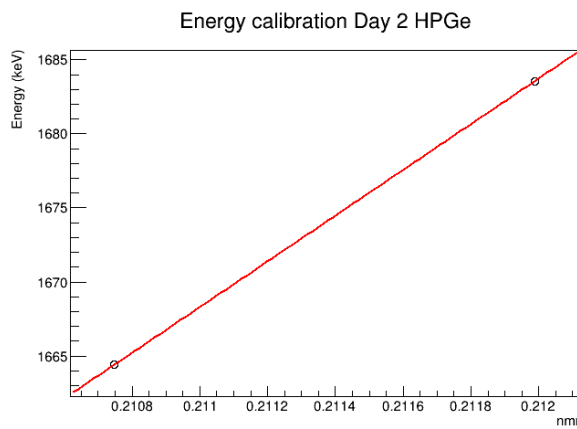


FIG. 20 Accelerator energy calibration (using HPGe, on 28/04/23).

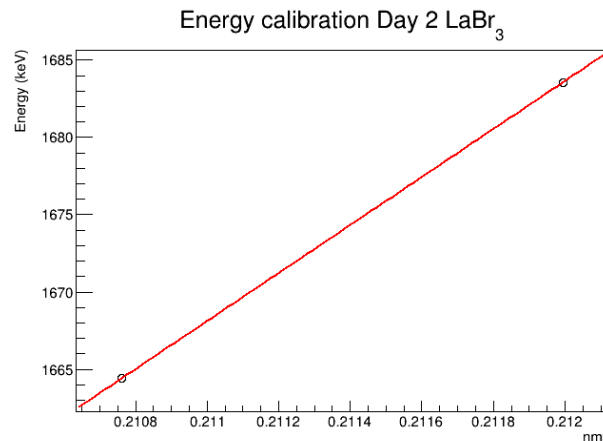


FIG. 21 Accelerator energy calibration (using LaBr₃, on 28/04/23).

Considering the calibrations performed within the same day, we can observe how they coincide and are clearly compatible (as expected, since otherwise it would have meant the malfunction of one of the two detectors), with values falling within the associated errors. It is therefore possible to calculate a weighted average to obtain a calibration for the first day and another for the second, as reported in TAB. 7.

Parameters	Calibration of 27/04/23	Calibration of 28/04/23
Slope [keV/nmr]	$(1.4083 \pm 0.0003)E+4$	$(1.550 \pm 0.014)E+4$
Intercept [keV]	$(-1.3015 \pm 0.0006)E+3$	$(-1.60 \pm 0.03)E+3$

TAB. 7 Daily calibration obtained from the weighted average of individual detectors.

In comparing calibrations obtained on different days, consistency is reduced (and compatibility of course is completely lost), which can be primarily attributed to two factors:

- Firstly, on the second day, a scan was conducted only of the second and third resonances, neglecting the first due to technical malfunctions of the equipment;
- Secondly, the linear behavior is a rough approximation, valid locally¹⁷ and considered here on a global level

¹⁷ Therefore, locally, the linear approximation of the conversion may exhibit different slopes between the region around 992 keV and that between 1664 and 1684 keV.

because only three data points are available. For a more accurate calibration, many more points should be taken into account, in order to utilize the precise expression that links the magnetic field and the beam energy.

- Thirdly, there may be fluctuations between different days, which will be discussed in the following paragraph.

E. Comparison

Therefore, having obtained the fitting parameters mentioned previously, it was not only possible to calibrate the accelerator but also to proceed with several observations. Initially, using the conversion tables provided by the laboratory, we were able to extract calibration fits for the regions of interest¹⁸, which are presented here in FIG. 22 and 23¹⁹.

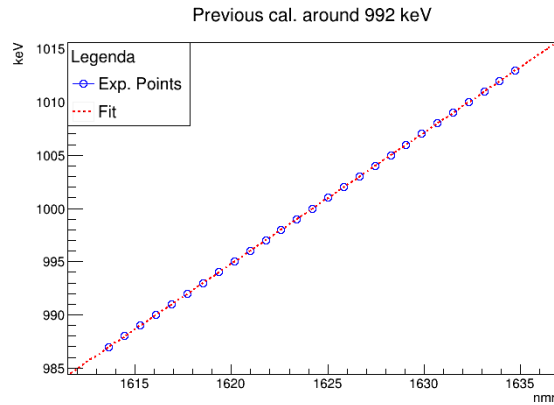


FIG. 22 Linear calibration around 992 keV, based on conversion table provided by the Lab.

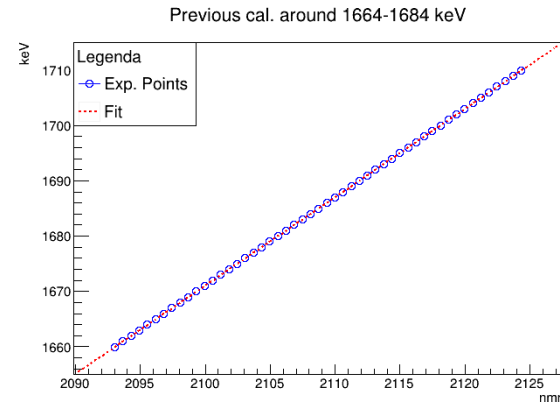


FIG. 23 Linear calibration around 1664-1684 keV, based on conversion table provided by the Lab.

	Slope [keV/10 ⁴ nmr]	Intercept [keV]	χ^2	Ndof
992 keV	1.2307 ± 0.0004	-998.9 ± 0.7	0.005	25
1664-1684 keV	1.5967 ± 0.0004	-1681.9 ± 0.9	0.042	49

TAB. 8 Parameters of linear calibration based on conversion table provided by the Lab.

Based on these previous calibrations, it is therefore possible to estimate the energy levels at which we detected the resonances²⁰, by determining the shift of the entire apparatus relative to the period since the last calibration.

Theoretical Energy [keV]	Measured Energy [keV]
DAY 1	
992	1005 ± 1
1664	1682 ± 1
1684	1702 ± 1
DAY 2	
1664	1683 ± 1
1684	1703 ± 1

TAB. 9 Energy shift measured by Lanthanum detector, considering the old calibration provided by the Lab.

As can be observed, for the first day, both detectors showed an energy shift of 13 keV for the first resonance, 18 keV for the second, and 17.5 keV for the third. On the second day, a shift of 19 keV was recorded for both resonances

¹⁸ As can be seen, a linear fit has been considered for each of the two intervals. This approach is justified by the fact that these intervals are small relative to the total range, within which a linear trend may not be universally applicable. Consequently, the relationship between the values indicated by the NMR and the beam energy can be considered linear with a good approximation.

¹⁹ As can be observed from the graphs and tables provided, in the calibration carried out by the laboratory, the NMR values are reported as being multiplied by a factor of 10⁴ compared to those displayed by the instrument (and which are considered in all other graphs in this study). This accounts for the unit of measurement associated with the slope of the fit.

²⁰ This is in reference to the old calibration.

Theoretical Energy [keV]	Measured Energy [keV]
DAY 1	
992	1005 ± 1
1664	1682 ± 1
1684	1702 ± 1
DAY 2	
1664	1683 ± 1
1684	1703 ± 1

TAB. 10 Energy shift measured by HPGe detector, considering the old calibration provided by the Lab.

at beam energies (E_p) of 1664 keV and 1684 keV. This indicates that the shift in energy is not constant (i.e., not merely a simple offset), but rather it increases with the energy of the beam. Moreover, slight differences are noted between the two days; for the second and third resonances, the shift varied by 1 keV from one day to the next. This latter behavior may be attributed to the human element involved in operating and preparing the accelerator each day, potentially causing minor fluctuations.

In addition to the aforementioned points, the analysis conducted in the previous paragraphs also enables the estimation of the width of the measured resonances (always considering the calibration provided by the laboratory). Indeed, starting from the arc-tangent fits described in the previous paragraph, it is possible to measure the resonance width by simply considering parameters c and g in the following manner:

$$\Gamma_c = \frac{2}{c}, \quad \Gamma_g = \frac{2}{g}$$

Consequently, the values estimated (considering always the conversion table provided by the laboratory) are presented in TAB. 11 and 12.

Theoretical Energy [keV]	Theoretical Width [keV]	Measured Width [keV]
DAY 1		
992	0.07	0.69 ± 0.03
1664	0.45	0.67 ± 0.07
1684	<0.2	1.03 ± 0.04
DAY 2		
1664	0.45	1.11 ± 0.08
1684	<0.2	0.44 ± 0.06

TAB. 11 Energy width measured by Lanthanum detector, considering the old calibration provided by the Lab.

Theoretical Energy [keV]	Theoretical Width [keV]	Measured Width [keV]
DAY 1		
992	0.07	0.9 ± 0.3
1664	0.45	1.0 ± 0.4
1684	<0.2	1.2 ± 0.3
DAY 2		
1664	0.45	0.3 ± 0.2
1684	<0.2	0.6 ± 0.2

TAB. 12 Energy width measured by HPGe detector, considering the old calibration provided by the Lab.

As can be observed, the values for HPGe are characterized by very high errors, likely due to lower statistics. However, relying on the values derived from Lanthanum, the following observations can be made:

- First and foremost, concerning the first resonance, it is noted that the value is significantly larger than the theoretical width, suggesting that the major contribution in this case may be attributed to the energy width of the accelerator.
- Regarding the other two resonances, there are differences observed between the two days, which could be due to issues with the cooling system of the magnet on the second day, potentially contributing to these variations. By focusing on the values recorded on the first day (even considering that, despite significant errors, they are

consistent with the values obtained with HPGe), it can be observed that for the resonance at $E_p = 1664$ keV, the measured width approaches the theoretical width (indicating that the contribution to the width from the accelerator seems to be mitigated), while for the resonance at $E_p = 1684$ keV, the same considerations seen for the first resonance apply.

From these observations, it is evident that for particularly narrow resonances, the contribution to the width is primarily due to the beam spread from the accelerator, whereas for wider resonances this contribution is less significant (as the values are closer), and consequently, the measured width is more consistent with the expected theoretical value²¹.

²¹ Considering that the various contributions to the resonance width (accelerator beam spread, theoretical width, etc.) add quadratically to each other [6].

IV. PART 2

For the second part of the experiment, measurements were conducted to determine the resonance strength of the reaction $^{14}\text{N}(\text{p},\gamma)^{15}\text{O}$ at beam energy $E_p = 1058$ keV, pertinent to the Carbon-Nitrogen-Oxygen (CNO) cycle. This reaction is crucial as it is the rate-limiting step, thereby governing the entire energy production process. As depicted in FIG. 24, the system under study exhibits three resonances of significant importance: a subthreshold resonance at $E_{CM} = -505$ keV, a narrow resonance at $E_{CM} = 259$ keV (corresponding to a proton beam energy $E_p = 278$ keV in the laboratory reference frame), and another at $E_{CM} = 987$ keV (corresponding to $E_p = 1058$ keV in the laboratory reference frame). Regarding the latter two, the second resonance has been recently measured by various experiments, while the final one is less known and is the focus of the current study. Indeed both energy ranges are essential to constrain the fit of the excitation function within the R-matrix framework and to obtain a reliable extrapolated S-factor at very low astrophysical energies [6].

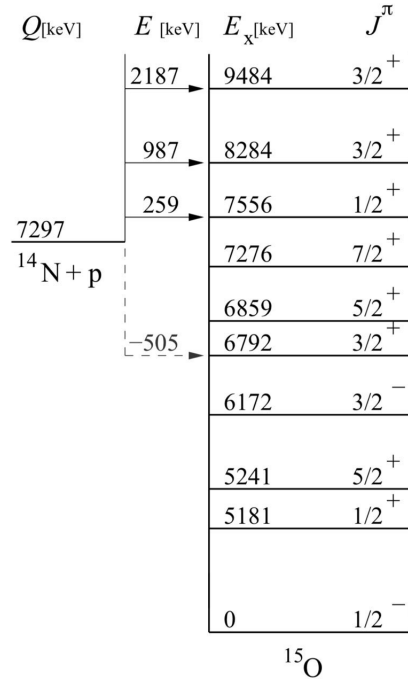


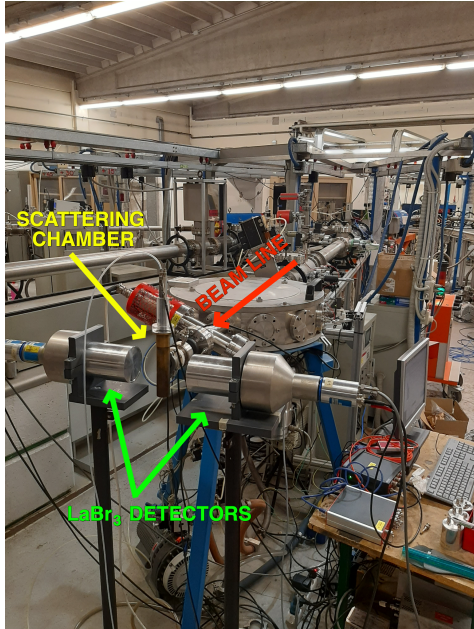
FIG. 24 Level scheme of excited states in ^{15}O , important for the $^{14}\text{N}(\text{p},\gamma)^{15}\text{O}$ reaction [6].

1. Experimental setup

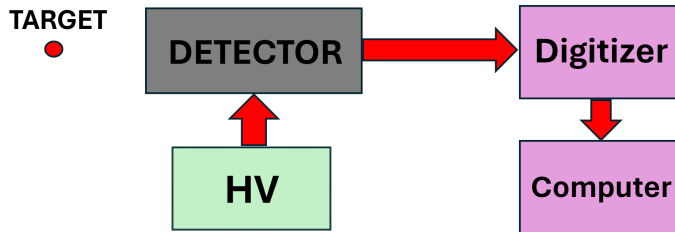
The experimental apparatus comprised the following components:

- The AN2000 accelerator (the entire facility, including magnets for bending the beam to select energy, and probes for measuring the magnetic field);
- A scattering chamber mounted specifically for this experiment at the end of the beam line positioned at -15 degrees;
- a tantalum nitride (TaN) target, produced by reactive sputtering²² on 0.2 mm thick Ta backings at LNL;
- two LaBr₃ detectors.

²² The sputtering process is a technique used to deposit thin films on solid substrates.

**FIG. 25** Detector setup.**FIG. 26** TaN target used for these measurements.

For this phase of the experiment, the AN2000 accelerator was used to generate a proton beam with energies below 2 MeV (consider the energy mentioned earlier when listing the reaction of interest). Also in this case, it is useful to determine the yield (see eq. 1) of the reaction to study the various details of the interested resonance. In order to measure the incident particles impinging on the target, a RBD's 9103 USB Picoammeter was used, connected to a laptop. This device measures dual-polarity DC current from picoamps to milliamps and data logging and graphing software is included for Microsoft Windows. In particular the 9103 works well in noisy environments. So this instrument returned for each measurement a file containing the current values recorded on the target every 0.05 s. Afterwards, this proton beam was accelerated towards the target, which was inserted inside the scattering chamber through a dedicated target holder. The latter allowed adjusting the height at which the target is positioned to ensure it was perfectly hit by the beam. Additionally, in this area, a compressed air tube had also been connected to prevent the environment inside the chamber from overheating. Another precaution was to connect a suppression of secondary electrons to the scattering chamber through an HW power supply model 3002 CANBERRA. This process was crucial to ensure that the collected data faithfully reflect the ongoing nuclear process and were not influenced by unwanted signals. In particular, secondary electrons are electrons released from interactions of the incident particles with the material of the detector or the target during the nuclear experiment, through processes of Coulomb scattering or ionization. The reaction (represented by the characteristic gamma rays emitted from the populated resonant states, forming the numerator of the yield) were then detected by the provided detectors, arranged as shown in FIG. 25. Both detectors were placed perpendicular and on both sides of the scattering chamber, at a distance from the center of approximately 10 cm, and they were equipped with a unique HV power supply (the electronic chain is described in the schematic representation of FIG. 27) provided by a CAEN 4 channel programmable HV power supply (Mod. N470) set at 600V.

**FIG. 27** Schematic representation of the analog chain.

Contrary to the setup used in the experiment conducted in the first part, during this one, both detectors were directly connected to the Digitizer (DT5781 from CAEN), and the acquisition was done using the CoMPASS software²³ in PHA mode. Finally, after arranging everything, the entire chamber was set into vacuum. For this purpose, a combination of primary (scroll pump) and secondary (turbomolecular pump) stage pumps was employed, achieving a vacuum within the chamber set to 10^{-6} mBar as in the first experience. In addition with respect to the previous occasion, this time, having installed the target along the beam line that extends beyond the main scattering chamber, it was necessary to use, with the previously mentioned pumps, also a Compact Full Range Gauge from Pfeiffer Vacuum to maintain the same pressure of 10^{-6} mBar.

2. Data acquisition

The experiment consisted in two steps; first of all a resonance scan in which the energy of the beam was varied in small increments (the gamma spectrum was acquired at each step to obtain the Υ), and then a long run at a specific E_p to determine later the resonance strength. The adopted procedure is the same described in section III.2, the only difference is that in this case, a broader resonance scan was performed, starting from significantly lower energies and ending at relatively higher energies compared to the one expected to obtain the resonance.

The data acquisition process lasted three days, during which the following activities were carried out:

- On the first day, after setting up the apparatus and setting the accelerator to an energy below that of the first mentioned resonance, a scan was conducted considering a wide range of E_p .
- On the second day, a fairly long acquisition was carried out, lasting several hours. This long run was necessary to obtain enough statistics for the photopeak at ~ 8 MeV, and to see the latter more defined and detailed compared to the background. In particular, to acquire this run, the beam energy E_p was set to approximately 1067 keV, which ensures being in the middle of the plateau of the Υ curve relative to this resonance. The two main reasons for setting the energy on the plateau are as follows; the yield is maximum and consequently is the integral to be determined, and then one is sure to acquire the entire resonance, making the following approximation possible: $\Upsilon \propto \omega\gamma$.
- On the third day, a simple measurement with sources for energy calibration of the detectors was carried out.

3. Data analysis

A. Detector energy calibration

As before, the first step of analysis is the energy calibration of both LaBr₃ detectors (LaBr_{3, ch0}, LaBr_{3, ch1}), in order to translate the units of the data acquisition system into the ordinary energy units (keV). For the latter purpose, the acquired spectra of two radioactive sources, ²²Na and ¹³⁷Cs, were used. In particular, in this phase, it was decided to consider an additional point, namely the energy at which the studied resonance occurs (~ 8.3 MeV), because it is a well-known value and can be clearly distinguished just looking at the spectrum (so, even in ch, arbitrary units). This was done to ensure a valid energy calibration even at energies far from the points derived from the previously mentioned sources. Then a Gaussian fit was performed for every peak, in order to get the centroids and their errors; these values are shown in TAB. 13:

	LaBr _{3, ch0} [keV]	LaBr _{3, ch1} [keV]
²² Na 511 keV	529.14 ± 0.02	370.37 ± 0.02
¹³⁷ Cs 662 keV	683.83 ± 0.14	479.51 ± 0.12
²² Na 1275 keV	1314.33 ± 0.06	929.43 ± 0.05
Resonance 8284 keV	8288 ± 1	6196.6 ± 1.9

TAB. 13 Centroids of every peak for each source.

Then a linear fit was executed for both detectors, such that:

²³ A DAQ software from CAEN able to implement a Multiparametric Data Acquisition for Physics Applications, capable to acquire energy, timing, and PSD spectra at the same time.

$$E_\gamma = a + bN_{ch}, \quad (15)$$

where E_γ represents the known values²⁴ of photopeak energies for the considered sources, N_{ch} is the position of the peak centroid in the units of the DAQ system and a and b are the fit parameters.

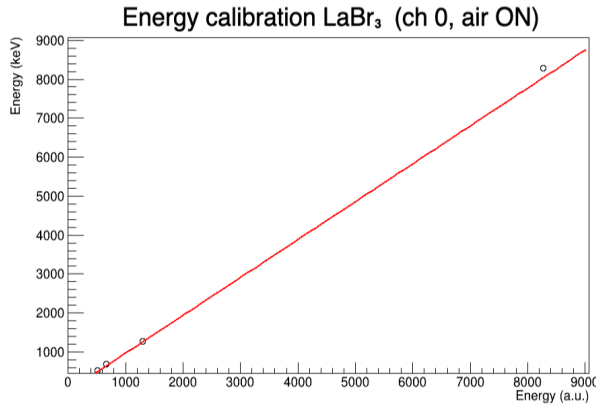


FIG. 28 Energy calibration fit of LaBr_{3, ch0} detector.

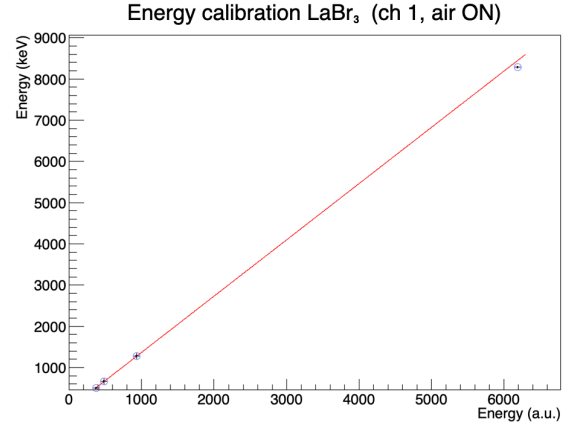


FIG. 29 Energy calibration fit of LaBr_{3, ch1} detector.

The obtained fit parameters are shown in TAB. 14.

	Slope [keV/ch]	Intercept [keV]
LaBr _{3, ch0}	0.97238 ± 0.00008	-3.51 ± 0.05
LaBr _{3, ch1}	1.36345 ± 0.00012	6.24 ± 0.06

TAB. 14 Parameters of energy calibration of both detectors.

B. Detector background evaluation

In this second phase of the experiment as well, to obtain a reliable value of the yield Υ , it is necessary to determine a reliable value of the integral of the area under the peak of the studied resonance (~ 8.3 MeV). In this case, the latter no longer falls within a critical energy range concerning the intrinsic background of the LaBr₃ detectors. Consequently, for each acquired spectrum, it was assumed that the background followed the trend of a second-degree polynomial, and its contribution was subtracted during various fitting operations on the peak of the studied resonance (see FIG. 30). Subsequently, to obtain the integral of the Gaussian peak, the parameters of the curve derived from the aforementioned fit were considered.

²⁴ The known values of the emission energies of ²²Na and ¹³⁷Cs are available on web site:http://www.lnhb.fr/nuclides/Na-22_tables.pdf, http://www.lnhb.fr/nuclides/Cs-137_tables.pdf.

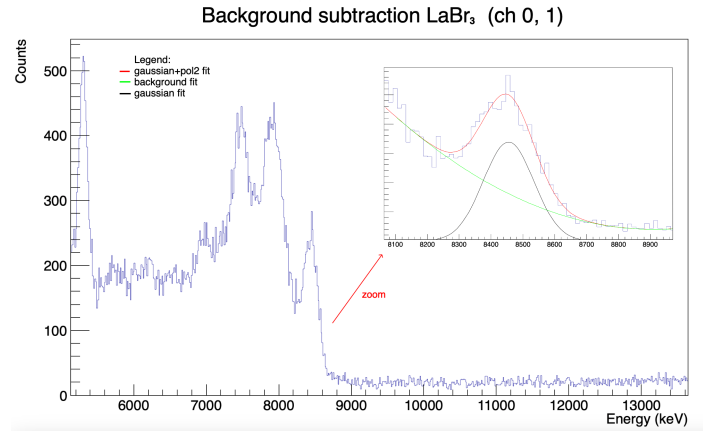


FIG. 30 LaBr₃ background subtraction from one of the acquired spectrum.

C. Accelerator calibration

Also during the second phase of the experiment, the energy calibration of the AN2000 accelerator was conducted because it was used another beam line. In this case, the well-known resonance of the reaction defined in the introduction of the section IV was exploited. Therefore, the Υ was calculated for each measurement referring to formula 11, although in this circumstance, it was used a RBD's 9103 USB Picoammeter to measure the current (μA) arriving on the target. Therefore, the latter returns for each measurement a file containing the current values recorded on the target every 0.05 s. Thus, it is necessary first to integrate these values over time, obtaining the total charge arrived on the target, which then needs to be normalized as follows:

$$N_c = \frac{charge_{tot} \cdot 10^{-6} \cdot 0.05}{1.6 \cdot 10^{-19}} \quad (16)$$

In particular, the error of RBD's 9103 USB Picoammeter can be considered negligible, so the only error source for the Υ derives from the calculation of the integral from each histogram.

Studying the reaction $^{14}\text{N}(\text{p},\gamma)^{15}\text{O}$, the Υ was calculated by analyzing the photon peak of about 8284 keV²⁵ for each spectrum acquired during the scan for both LaBr₃detectors (see appendix A). Then, the Υ values obtained were plotted as a function of the corresponding NMR probe values, and a fit was performed with a double arc-tangent function:

$$f(x) = a + b \cdot atan(c \cdot (x + d)) - (e + f \cdot atan(g \cdot (x + h))) \quad (17)$$

this particular shape is because the target is considered finite, even if considerably bigger with respect to the width of the studied resonance. In fact in this case, by further increasing the energy of the proton beam, it is possible to reach the end of the target, even going beyond it.

Parameters	LaBr _{3, ch0}	LaBr _{3, ch1}
a	(2.9±0.2)E-2	(2±2)E-2
b	(1.7±0.4)E-2	(2.9±0.8)E-2
c [1/nmr]	(1.9±1.3)E+3	(2.3±1.7)E+3
d [nmr]	(-2.4182±0.0016)E-1	(-2.4196±0.0014)E-1
e	(1.1±0.2)E-2	(4±2)E-3
f	(1.2±0.2)E-2	(2.3±0.5)E-2
g [1/nmr]	(7±1)E+3	(4±3)E+3
h [nmr]	(-2.4587±0.0015)E-1	(-2.4443±0.0013)E-1
χ^2	0.5	2.0

TAB. 15 Double arc-tangent fit parameters for both detectors.

²⁵ Since the decay with a single photon emitted at ~8284 keV at the one specific energy of the proton beam was the main branch (>50%), according to <https://www.nndc.bnl.gov/>.

Observing TAB. 15, it can be noticed that for both detectors, a χ^2 value quite in line with the Ndof is obtained, therefore the errors associated with the fitted points can be considered adequate. This is probably due to the new background subtraction process used for the LaBr₃, which leads to a propagation of errors associated with the parameters of the fits performed on the peak, and affects the error associated with the calculated integrals.

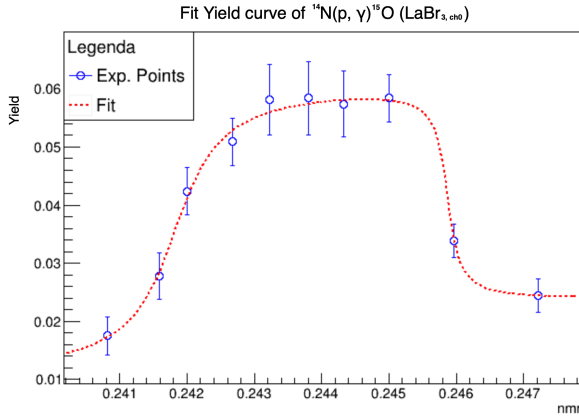


FIG. 31 Double arc-tangent fit of the Yield curve for $E_\gamma = 8284$ keV (LaBr_{3, ch0}).

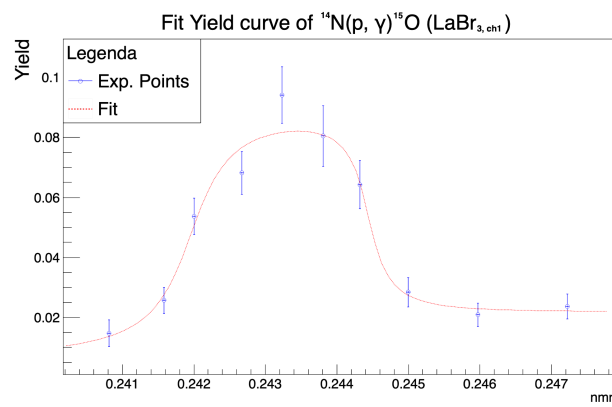


FIG. 32 Double arc-tangent fit of the Yield curve for $E_\gamma = 8284$ keV (LaBr_{3, ch1}).

Looking at both FIG. 31 and 32, some observations can be done:

- Firstly, the information that can be derived from these graphs indicates the finite width of the target. Specifically, the thickness that can induce the reaction of interest is concentrated in a thin layer that has formed on the surface. Once this layer is surpassed by the protons from the beam, for instance with energies too high to achieve the desired reaction within it, it can no longer produce any reaction. Therefore, based on the yield, it is possible to probe the target thickness expressed in energy units (corresponding to the energy range of the high plateau). In this instance, the layer containing TaN corresponds to an energy width between 20 and 30 keV, which aligns with theoretical expectations;
- Secondly, there is a difference in the steepness of the ascent and descent of the double arc-tangent fit. In fact the ascent appears to be smoother, while the descent is extremely steep, although generally the opposite situation should occur. This strange particularity likely occurs because the descent region is poorly mapped, as only a few measurement points were acquired since it was not the actual region of interest. Therefore, it is not known what the actual trend of the descent is. Then another reason is that the target is not uniform, in fact it has different layers of different materials;
- In conclusion, it can be observed that the second flat trend of the graph appears higher than the initial one. This phenomenon may primarily be attributed to the same reason discussed in the previous section. Additionally, the target formation process does not seem capable of producing a distinct separation between the initial substrate and the TaN thickness. Instead, it exhibits a gradient-like behavior, potentially allowing some nitrogen atoms to penetrate deeper layers.

In this instance as well, the parameter **d** represents the flex of the arc-tangent, i.e. the value E_p at which resonance occurs, while **c** is a parameter from which the width of the resonance can be derived. Then, referring to the fit parameter **d**, a check of the official calibration related to the beam line used during the second phase of the experiment was performed. In this instance, it was observed that according to the calibration provided by the laboratory's conversion table, the position of the flex corresponds to 1053 ± 2 keV²⁶ (obtained in the same way as in Part 1 experiment). So, in conclusion, it was found that the value of the NMR probe corresponding to the flex actually almost coincides with the energy set by the control panel (referring to the official conversion). Therefore, it was not necessary to recalibrate that beam line as during the first phase of the experiment, since the official calibration can still be considered valid. Finally, it can be hypothesized that this difference between the various beam lines is due to an angular coefficient to be determined.

²⁶ Therefore, unlike the previous case, we now observe a more contained shift, which is no longer forward but backward.

D. Strength measurement

Once the behavior of the yield curve was determined, it was possible to proceed by setting the beam energy to the midpoint of the upper plateau. This step was taken to ensure that the entire resonance curve corresponding to the reaction of interest was fully captured and, therefore, to ensure that one is working under the condition where the energy width of the target is bigger than the resonance width²⁷. In this case the total width of the resonance is small compared to the energy loss (or width) in the target ($\Delta E \gg \Gamma$) so, setting the beam energy as mentioned just before, we ensure that the target extends over all energies where the resonant cross section (assuming that it obeys the Breit-Wigner description mentioned in the introduction) is non-negligible. This allows us to apply the classical definition for the thick target yield Υ_∞ [6]. Upon setting the beam energy to meet the desired conditions, as described in the section on experimental setup, we conducted a long data collection run to accumulate sufficient statistics. As discussed earlier, the expression for the yield will be given by the formula presented in the initial introductory chapter (eq. 9, obtained approximating the target as infinitely thick). This formula was manipulated to isolate the resonance strength, resulting in:

$$\omega\gamma = \frac{2\epsilon_r \Upsilon_\infty}{\lambda^2 \beta}$$

In this revised version, an additional β term appears, which accounts for aspects previously not considered, namely the absolute photopeak efficiency and the branching ratio of the excited state being populated. From this expression, considering the excited state of ^{15}O populated by this reaction, it was chosen to focus not only to the gamma ray of $E_\gamma = 8283$ keV, but also to another frequent gamma of $E_\gamma = 3043$ keV²⁸. The various terms were derived as follows:

- λ (**De Broglie wavelength**): Using its formula for the reduced system, it is given by:

$$\lambda^2 = 4\pi^2 \cdot \frac{\hbar^2}{2m_r E_r} = 4\pi^2 \cdot \hbar^2 \cdot \frac{1}{2 \cdot \frac{m_p m_N}{m_p + m_N} \cdot E_{\text{CM}}} = 8.967 \cdot 10^{-24} \text{ cm}^2$$

- ϵ_r (**effective stopping power**): Given that this involves a composite system, including Tantalum nuclei, its expression is provided in the initial chapter (see eq. 4 for compound targets).

$$\epsilon_r = \epsilon_N(E_p) + \epsilon_{\text{Ta}}(E_p) \cdot \frac{n_{\text{Ta}}}{n_N}$$

To calculate this value, the SRIM software code was used, while the stoichiometric values were based on literature. This allowed to estimate the following value for this term:

$$\epsilon_r = 20.5 \frac{\text{eV}}{10^{15} \text{ atoms/cm}^2}$$

In this case, given that fluctuations may occur in this number, it has been decided to maintain a substantial error margin of 10% to accommodate potential variations in the selected value.

- Regarding the β **parameters** (one for each of the two gamma rays considered), since there are no efficiency measurements available for the gamma detectors at the energies relevant to the reaction under investigation, simulations previously performed [2] were utilized. These simulations provided the values for absolute photopeak efficiency (first terms in brackets). For the branching ratios (second terms in brackets), reliance was placed on the values reported by the National Nuclear Data Center at Brookhaven, enabling the acquisition of:

$$\beta_{8 \text{ MeV, det-0}} = \left(\frac{0.5}{100}\right) \cdot \left(\frac{53.2}{100}\right) = 2.7 \cdot 10^{-3} \quad \beta_{3 \text{ MeV, det-0}} = \left(\frac{0.9}{100}\right) \cdot \left(\frac{42.2}{100}\right) = 3.8 \cdot 10^{-3}$$

$$\beta_{8 \text{ MeV, det-1}} = \left(\frac{0.5}{100}\right) \cdot \left(\frac{53.2}{100}\right) = 2.7 \cdot 10^{-3} \quad \beta_{3 \text{ MeV, det-1}} = \left(\frac{1.0}{100}\right) \cdot \left(\frac{42.2}{100}\right) = 3.8 \cdot 10^{-3}$$

Since in this case the estimation of the absolute photopeak efficiency relied on a graph from the recently referenced work, an error of 0.05% has been considered for the selected value, due to the uncertainty associated with the extrapolation performed.

²⁷ Indeed, when a beam with energy slightly higher than the resonance impinges on an extended target, it produces resonant reactions at a particular depth inside the target, after the ions underwent some energy loss until the resonance energy is reached

²⁸ According to data from the NNDC site, the 8 MeV gamma ray is emitted in 53.2% of the decay events, while the 3 MeV gamma ray is emitted in 42.2% of the events.

- **Yield:** As for this value, its expression remains the same as seen in previous chapters. Considering the instruments used in this experiment, which enable us to measure the current generated by the incident beam, the yield takes the following form:

$$\Upsilon_{\infty} = \frac{N_{peak}}{\frac{N_{scaler} \cdot 10^{-6} \cdot 0.05}{e}}$$

Where N_{peak} represents the integral of the Gaussian at the photopeak, and N_{scaler} is the integral of the values measured by the ammeter throughout the duration of the run. The subsequent multiplicative terms are used to obtain the total number of protons that have passed through, and thus impinged on, the target²⁹. For this value, the associated error was derived simply by error propagation originating from the Gaussian fit applied to the histogram peak of our interest.

The resonance strength values obtained are thus reported in TAB. 16.

	$\omega\gamma_3 \text{ MeV}$ [eV]	$\omega\gamma_8 \text{ MeV}$ [eV]
Det-0	0.26 ± 0.03	0.38 ± 0.04
Det-1	0.30 ± 0.02	0.43 ± 0.05

TAB. 16 Resonance strength measured.

As can be observed, the error in this case is significant. This arises from the propagation method used, but it is important to clarify in the error estimates that the approximate nature of the measurement conducted was also considered. In addition to the efficiency inferred from graphs derived from simulations, it is also necessary to account for significant effects that were not considered, such as the summing effect. Consequently, the value obtained requires a sufficiently large error margin to reflect all the approximations made. Among the most recent results in the literature, the reference value is reported to be $\omega\gamma = 0.353 \pm 0.018$ eV. By comparing this value with the measurements conducted in this study, we obtain the following compatibility indices (TAB. 17).

	$\omega\gamma_3 \text{ MeV}$	$\omega\gamma_8 \text{ MeV}$
Det-0	2.8	0.6
Det-1	1.9	1.5

TAB. 17 Resonance strengths' compatibilities with the reference value.

From the latest values obtained, several observations can be made:

- First and foremost, concerning the measurements taken with the first Lanthanum detector, we note that the measurement at 8 MeV gamma-ray appears particularly consistent, in contrast to the measurement at 3 MeV gamma-ray, which is notably less so. This indicates primarily the successful acquisition of the measurement for the former value, confirming the data present in literature. Furthermore, it suggests that for the 3 MeV gamma-ray, certain noise factors might have deteriorated the estimation (it is important to consider that we are still in a region where the intrinsic background of Lanthanum is present);
- Regarding the estimates obtained from the other detector (Det-1), it is observed that while they display the same behavior described for the first detector, the estimation of the resonance strength from the 8 MeV gamma-ray is poorer compared to that obtained with the first detector. This finding aligns with expectations, given that this detector had already been found to be less effective, likely due to its deteriorated state.

²⁹ The 10^{-6} factor is due to the fact that the current is measured in μA , the factor of 0.05, instead, is attributed to the measurement of current being taken every 0.05 seconds; therefore, it serves as a necessary multiplicative factor to integrate the current and obtain a charge.

V. CONCLUSIONS

To conclude, the following activities were conducted during this project, which was divided into two distinct experiments. For the first part:

- Energy calibration was performed for both the Germanium and Lanthanum detectors. After that, scans of two reactions were carried out to determine the yield behavior for the three resonances of interest.
- After the yield trends were established and fitted, the derived parameters revealed significant shifts in energy measurements on the first day: 13 keV for the first resonance at $E_p = 992$ keV, 18 keV for the second at $E_p = 1664$ keV, and 17.5 keV for the third at $E_p = 1684$ keV.
- On the second day, both resonances at E_p equals to 1664 and 1684 keV exhibited a shift of 19 keV.

These findings highlight discrepancies with the old calibration of the beam line at -60 degrees, as represented by the conversion tables provided by the laboratory. Variations in energy shifts depended on the beam energy, and changes from day to day were noted, influenced by human factors involved in daily operations of the setup. Furthermore, the resonances widths were estimated, indicating that for the first reaction and the second resonance of the second reaction they matched the beam width due to the accelerator, while for first resonance of the second reaction there was a convergence of resonance and beam widths due to their similar values. The measures described are clearly aimed at assessing the current state of the conversion tables in the laboratory and gaining an understanding of how much they have changed. However, these cannot be considered a comprehensive calibration, since they involve only three points and thus are insufficient to accurately represent the global relationship between NMR values and beam energy. Nonetheless, potential improvements could involve the use of additional resonances to obtain more data points, thereby providing a more complete overview of the actual calibration.

For the second part, instead:

- After the usual energy calibration, this time for two identical Lanthanum Bromide detectors, a scan was performed at increasing energies (around the expected resonance value) to estimate the yield trend. The fit of this yield curve showed better alignment with the laboratory-provided conversion table values at a -15° angle line.
- Having estimated the position and the finite length of the curve's leading edge, the beam energy was set to the midpoint of this range for a long run to measure the resonance strength, which was consistent with values reported in the literature. Specifically, the best result was observed for the detector of channel 0 with 8 MeV gamma rays, consistent with expectations since this detector is the least outdated and those radiations have the best branching ratio for the studied energy level.

Despite the successful measurements, there are several areas for improvement in this second part to achieve better accuracy and more reliable estimates:

- Firstly, by extending the data collection duration to optimize statistical significance;
- Considering contributions from the summing effect, which could alter the measured results;
- Increasing the input current to reduce the time needed to achieve sufficient statistics.

REFERENCES

- [1] A. Caciolli. *Lecture Notes for the Course of Nuclear Astrophysics*. Università degli studi di Padova, 2023.
- [2] L. Cavezza. Study of a gamma detection system's efficiency using monte carlo simulations, 2023.
- [3] Gordon R. Gilmore. *Practical Gamma-ray Spectrometry - 2nd ed.* Wiley, 2008.
- [4] Christian Iliadis. *Nuclear Physics of Stars*. Wiley, 2007.
- [5] Glenn F. Knoll. *Radiation detection and measurement - 3rd ed.* Wiley, 2000.
- [6] M. Marta. *The $^{14}N(p,\gamma)^{15}O$ reaction studied at low and high beam energy*. PhD thesis, Technischen Universität Dresden, 2011.
- [7] M. Mazzocco. *Lecture Notes for the Course of Radioactivity and Nuclear Measurements*. Università degli studi di Padova, 2023.
- [8] V. Rigato. The interdisciplinary laboratory of the an2000 van de graaff accelerator: Status and perspective. *LNL Annual Report*, 2009.

Appendix

Appendix A: Tables

NMR probe	Charge [10^{-10} C]	HPGe detector		LaBr_3 detector	
		Integral	Yield ($\cdot 10^{-13}$)	Integral	Yield ($\cdot 10^{-13}$)
0.161601	1937126	180 ± 20	1.52 ± 0.16	9700 ± 100	80.4 ± 0.9
0.1620065	2143853	210 ± 20	1.58 ± 0.15	10800 ± 100	80.7 ± 0.9
0.1624148	1241894	110 ± 10	1.40 ± 0.16	6220 ± 90	80.1 ± 1.2
0.162658	2257586	220 ± 20	1.55 ± 0.14	11500 ± 100	81.5 ± 0.9
0.162758	3517177	350 ± 20	1.59 ± 0.11	18100 ± 200	82.2 ± 0.7
0.1628214	2624152	350 ± 20	2.14 ± 0.15	17200 ± 100	104.7 ± 0.9
0.1628535	2295052	360 ± 20	2.48 ± 0.17	19100 ± 100	132.9 ± 1.0
0.1629005	1738153	330 ± 20	3.0 ± 0.2	17000 ± 100	156.5 ± 1.3
0.1629838	1561189	290 ± 20	2.9 ± 0.2	16200 ± 100	166.4 ± 1.4
0.1630295	1978910	380 ± 20	3.10 ± 0.2	20600 ± 200	166.6 ± 1.2
0.163082	1869546	390 ± 30	3.4 ± 0.2	19800 ± 100	169.9 ± 1.3
0.1632974	1542355	330 ± 20	3.4 ± 0.2	16300 ± 100	169.0 ± 1.4

TAB. 18 Useful values for the Yield curve of the resonances at $E_p \sim 992$ keV (HPGe and LaBr_3 detector, 27/04/23).

NMR probe	Charge [10^{-10} C]	HPGe detector		LaBr_3 detector	
		Integral	Yield ($\cdot 10^{-12}$)	Integral	Yield ($\cdot 10^{-12}$)
0.209559	1893720	2300 ± 60	1.94 ± 0.05	79000 ± 400	66.7 ± 0.3
0.2097548	1140608	1410 ± 50	1.98 ± 0.07	47800 ± 300	67.1 ± 0.4
0.2098615	1190864	1400 ± 50	1.88 ± 0.06	50700 ± 300	68.1 ± 0.4
0.2099905	1108183	1370 ± 50	1.97 ± 0.07	47300 ± 300	68.3 ± 0.4
0.2101174	1182356	1370 ± 50	1.86 ± 0.06	50400 ± 300	68.2 ± 0.4
0.2103124	1129905	1350 ± 50	1.91 ± 0.07	48600 ± 300	68.7 ± 0.4
0.2104313	1065480	1330 ± 50	2.00 ± 0.07	45700 ± 300	68.6 ± 0.4
0.210564	1035732	1300 ± 40	2.01 ± 0.07	45300 ± 300	69.9 ± 0.4
0.210614	1066567	1380 ± 50	2.07 ± 0.07	47300 ± 300	71.0 ± 0.4
0.2106817	898428	1350 ± 50	2.40 ± 0.08	49000 ± 300	87.2 ± 0.5
0.2107497	770106	1370 ± 50	2.85 ± 0.09	49300 ± 300	102.4 ± 0.6
0.21082	720700	1360 ± 40	3.03 ± 0.10	48700 ± 300	108.0 ± 0.6
0.2110535	705868	1330 ± 50	3.02 ± 0.11	49000 ± 300	111.0 ± 0.6
0.2113686	725200	1370 ± 50	3.02 ± 0.10	49900 ± 300	110.0 ± 0.6
0.21169	734076	1370 ± 50	2.98 ± 0.11	50300 ± 300	109.6 ± 0.6
0.211878	605159	1380 ± 50	3.64 ± 0.12	51800 ± 300	136.8 ± 0.7
0.2119083	509234	1330 ± 50	4.18 ± 0.14	49900 ± 300	156.7 ± 0.8
0.2119278	475936	1330 ± 50	4.46 ± 0.16	50200 ± 300	168.9 ± 0.9
0.2119938	416187	1340 ± 50	5.14 ± 0.18	50100 ± 300	192.8 ± 1.0
0.212079	416134	1370 ± 40	5.25 ± 0.17	51100 ± 300	196.3 ± 1.0
0.212248	408586	1380 ± 40	5.41 ± 0.17	50800 ± 300	198.9 ± 1.0

TAB. 19 Useful values for the Yield curve of the resonances at of $E_{p1} \sim 1664$ keV and the other at $E_{p2} \sim 1684$ keV (HPGe and LaBr_3 detector, 27/04/23).

NMR probe	Charge [10^{-10} C]	HPGe detector		LaBr_3 detector	
		Integral	Yield ($\cdot 10^{-12}$)	Integral	Yield ($\cdot 10^{-12}$)
0.209583	1173742	1400 ± 50	1.91 ± 0.07	49700 ± 300	67.8 ± 0.4
] 0.210172	2139813	2620 ± 70	1.96 ± 0.05	92300 ± 400	69.0 ± 0.3
0.2104385	1009657	1160 ± 40	1.84 ± 0.07	45000 ± 300	71.3 ± 0.5
0.210621	844707	1090 ± 40	2.06 ± 0.08	37500 ± 300	71.1 ± 0.5
0.210685	1026742	1250 ± 50	1.95 ± 0.07	47200 ± 300	73.6 ± 0.5
0.2107485	697916	1080 ± 40	2.47 ± 0.10	37800 ± 300	86.6 ± 0.6
0.210808	565525	1010 ± 40	2.86 ± 0.11	36400 ± 200	102.9 ± 0.7
0.2108698	537351	1010 ± 40	3.01 ± 0.12	36400 ± 200	108.3 ± 0.7
0.210992	570163	1030 ± 40	2.90 ± 0.11	39900 ± 300	111.9 ± 0.7
0.211506	544313	1040 ± 40	3.04 ± 0.12	38000 ± 300	111.6 ± 0.8
0.2118745	545682	1010 ± 40	2.96 ± 0.12	39500 ± 300	115.9 ± 0.8
0.2119272	548636	1100 ± 40	3.21 ± 0.12	40300 ± 300	117.4 ± 0.8
0.2120025	344292	990 ± 40	4.61 ± 0.19	37100 ± 200	172.2 ± 1.1
0.2120638	408953	1280 ± 40	5.00 ± 0.18	50100 ± 300	195.9 ± 1.1
0.2121151	362765	1190 ± 40	5.23 ± 0.19	44900 ± 300	198.0 ± 1.1
0.2122478	306244	1020 ± 40	5.3 ± 0.2	37900 ± 200	198.2 ± 1.2
0.212434	301184	1010 ± 40	5.4 ± 0.2	37900 ± 200	201.2 ± 1.2

TAB. 20 Useful values for the Yield curve of the resonances at of $E_{p1} \sim 1664$ keV and the other at $E_{p2} \sim 1684$ keV (HPGe and LaBr_3 detector, 28/04/23).

NMR probe	Charge [μA in 0.05s]	$\text{LaBr}_{3,\text{ch}0}$ detector		$\text{LaBr}_{3,\text{ch}1}$ detector	
		Integral	Yield ($\cdot 10^{-2}$)	Integral	Yield ($\cdot 10^{-2}$)
0.240815	7235	130 ± 20	1.8 ± 0.3	110 ± 30	1.5 ± 0.4
0.241583	7925.583	220 ± 30	2.8 ± 0.4	200 ± 30	2.6 ± 0.4
0.242006	8101.9886	340 ± 30	4.2 ± 0.4	430 ± 50	5.4 ± 0.6
0.2426723	8529.9512	430 ± 30	5.1 ± 0.4	580 ± 60	6.8 ± 0.7
0.2432322	5551.0542	320 ± 30	5.8 ± 0.6	522 ± 50	9.4 ± 0.9
0.2438066	4971.0854	290 ± 30	5.8 ± 0.6	400 ± 50	8.1 ± 1.0
0.244322	6068.1371	350 ± 30	5.7 ± 0.6	390 ± 50	6.4 ± 0.8
0.2449961	11677	680 ± 50	5.8 ± 0.4	330 ± 60	2.8 ± 0.5
0.2459711	15708.1374	530 ± 40	3.4 ± 0.3	330 ± 60	2.1 ± 0.4
0.24722	15708	380 ± 50	2.4 ± 0.3	370 ± 70	2.4 ± 0.4

TAB. 21 Useful values for the Yield curve of the resonances at $E_p \sim 1058$ keV (LaBr_3 detectors). In this case, it can be noted that the values of Υ have a different order of magnitude compared to those calculated for the first phase of the experiment. This difference is due to the fact that in this latter phase, the total charge was not normalized, and therefore the raw values were used, as the only reason for redoing this analysis was to perform a quick check of the official calibration on this new beam line.